

FULL PAPER

Open Access

# Geotechnical behavior of mudstones from the Shimanto and Boso accretionary complexes, and implications for the Nankai accretionary prism

Kai Schumann<sup>1\*</sup>, Jan H Behrmann<sup>1</sup>, Michael Stipp<sup>1</sup>, Yuzuru Yamamoto<sup>2</sup>, Yujin Kitamura<sup>3</sup> and Christof Lemp<sup>4</sup>

## Abstract

Triaxial shear tests on mudstone samples from the Shimanto Belt and the Boso accretionary complexes (SW Japan and central Japan) were carried out. Pre-exhumation burial depths in the two paleo-accretionary prisms were up to 9,000 m and about 1,000 m for the Shimanto and the Boso samples, respectively. Three methods were applied: (1) pressure stepping tests at increasing confining pressures between 25 and 65 MPa and pore pressures between 20 and 52 MPa; (2) constant confining pressure tests at 55 and 65 MPa, with stepwise pore pressure decrease from 80% to 50% and 25%, and from 90% to 60% and 30% of the confining pressure; and (3) a cyclic loading test on one sample from Boso (19 cycles to 70-MPa differential stress). After some contraction due to pressurization in the first cycles, the sample showed tendencies to creep rather than to fracture.

Effective shear parameters show that angles of internal friction between 30° and 50° are in part quite high in both sample subsets, and ranges of cohesion are between about 2 and 6 MPa (Boso) and 13 and >30 MPa (Shimanto). The mechanical results from these paleo-accretionary prisms are taken to constrain the shear parameters of rocks in the deeper parts of the present Nankai accretionary wedge and forearc. Static friction resembles results from experiments on a wide range of phyllosilicate-quartz-feldspar gouges and shows that the forearc is composed of relatively strong rock. Cohesion increase due to diagenesis and/or very low grade metamorphism is of overriding importance and probably permits stresses of up to 18 MPa to be transmitted to the updip end of the seismogenic zone at depth and 5 to 13 MPa to the backstop of the actively deforming frontal prism.

**Keywords:** Shimanto Belt; Boso accretionary prism; Nankai; IODP; Triaxial shear test; Mudstone; Subduction zone

## Background

Subduction zones are tectonically highly active regions on Earth and are known to generate large earthquakes by thrust faulting (for reviews on subduction zones, see von Huene and Scholl 1991; Saffer and Tobin 2011). Subduction zone earthquakes are caused by movements on the so-called plate boundary thrust in the seismogenic zone (e.g., Byrne et al. 1988; Scholz 1998; Moore and Saffer 2001) and/or by operation of splay faults (e.g., Park et al. 2002; Moore et al. 2007; Park and Kodaira 2012) further up in the thrust sequence. Splay faulting plays a critical role in the building of accretionary wedges, and clay-rich sediments usually act as décollement horizon in the tectonic

stacking process. Different hypotheses on the updip limit of the seismogenic zone exist. The presently most popular idea is that of Hyndman and Wang (1993), who state that temperature-controlled dehydration of clays at 100°C to 150°C causes a change in frictional properties. While clay dehydration is an important process without any doubt, there must be other factors that control the strength of accreted and subducted sediments. Most important is compaction during progressive burial, and cementation processes leading to lithification, be it under diagenetic or very low grade metamorphic conditions (e.g., Kimura and Ludden 1995; Moore and Saffer 2001; Matsumura et al. 2003; Saffer and Marone 2003; Morgan and Ask 2004; Kimura et al. 2007; Saffer and Tobin 2011). This increases cohesion, which apart from friction is the most important parameter governing the stresses that can be transmitted through accreted rock piles under horizontal loading.

\* Correspondence: kaschumann@geomar.de

<sup>1</sup>Marine Geodynamics, GEOMAR Helmholtz Centre for Ocean Research Kiel, Wischhofstr. 1-3, Kiel, Germany

Full list of author information is available at the end of the article

This means that the changing physical properties of clay-rich rocks, such as porosity, state of consolidation, mineral fabrics, and cementation, are instrumental in controlling seismicity (e.g., Scholz 1998; Moore and Saffer 2001) and determining the transition from stable frictional sliding behavior to unstable stick slip at convergent plate boundaries (e.g., Byrne et al. 1988; Vrolijk 1990; Hyndman et al. 1995; Oleskevich et al. 1999; Moore and Saffer 2001; Kimura et al. 2007).

Earthquakes are the result of a sudden stress release along a slip surface (e.g., Reid 1911; Brace and Byerlee 1966; Scholz 1998). The common assumption is that earthquakes occur on pre-existing faults and interfaces instead of newly generated faults. Thus, stress release along a slip surface should be purely a frictional phenomenon (Scholz 1998). However, faulted rocks at depth change their physical properties during interseismic diagenesis and healing, involving cementation and change in pore space and pore connectivity. The role and result of these processes needs to be quantified for a better understanding of earthquake generation in accretionary prisms. This lends justification to the approach to study samples of rocks, which have experienced a burial and diagenetic or metamorphic history comparable to those hosting the seismogenic zone at depth.

Here, we present the results of a series of tests on rock samples from tectonically exhumed accretionary complexes near the shore of SW Japan (Figure 1). These probably have been present in plate boundary thrusts and splay faults under triaxial stress conditions and can be taken as mechanical analogues for rock now at the updip end of the seismogenic zone. Drilling and instrumenting such rocks and structures *in situ* is the key objective of the ongoing NanTroSEIZE drilling project (e.g., Tobin and Kinoshita 2006a, b; Kuramoto et al. 2008) of the Integrated Ocean Drilling Program (IODP). The plan is to reach an active splay fault and the plate boundary thrust at the Nankai accretionary prism off SW Japan at depths up to 6,000 m below sea floor (see seismic cross section in Figure 2). Coring of both fault zones has not been achieved to date, and especially recovering samples suited for triaxial testing is likely to be an arduous task once the plate boundary and/or megasplay faults have been reached by the drilling. For this reason, we chose the strategy to sample rocks from analogous stratigraphic and/or structural contexts in two nearby fossil accretionary prisms: the Shimanto Belt along the coast of Shikoku Island (Figure 1B) and the Boso accretionary prism on the Boso Peninsula of Honshu Island (Figure 1C,D). The two sampling areas represent pre-exhumation burial depths of 7.8 to 9 km (Shimanto; e.g., Underwood et al. 1993b) and approximately 1,000 m (Boso; e.g., Yamamoto et al. 2005). Complementary to both data sets, triaxial test results of a suite of samples from the shallowest parts of the Nankai

accretionary prism (Stipp et al. 2013) are included in the discussion here to provide cohesion and friction information. The Nankai samples were recovered from the upper approximately 130 m of the accretionary prism by drilling during IODP Expeditions 315 and 316 southeast of Kii Peninsula (Figure 1A,E). The combination of geomechanical data from all three sample sets spans the complete depth range down to the upper part of the seismogenic zone and provides the opportunity to correlate near-surface mechanical properties (Nankai) down to approximately 9-km depth (Shimanto Belt analogues). We will attempt to use the data to make some predictions on the state of stress and conditions for the failure of the Nankai accretionary prism as a whole.

### Geological setting of the Shimanto Belt and Boso accretionary complex

The rocks sampled from the Shimanto Belt could serve as analogues for rocks now found at seismogenic zone depths at Nankai (Figure 2). The Shimanto Belt is approximately parallel to the Nankai Trough (e.g., Taira et al. 1992; Moore and Saffer 2001; Kawabata et al. 2007), and was sampled along the coastline of eastern Shikoku Island (Figure 1B). The depositional ages of the sediments decrease from north to south (Taira et al. 1988). The Shimanto Belt is divided by the Aki Tectonic Line into a northern Cretaceous part and a southern Tertiary part (e.g., Kumon 1983; Underwood et al. 1993c; DiTullio and Hada 1993). Samples in the present study only come from the Tertiary part. Overviews of the Shimanto stratigraphy are given by Taira et al. (1982), Aitchison (1986), Hibbard et al. (1992), or Underwood et al. (1993c). On the Muroto Peninsula, the Shimanto Belt is subdivided into the Eocene to Oligocene Murotohanto Group in the north and the Oligocene to Miocene Nabae Group in the south (Aitchison 1986; Underwood et al. 1992). Both groups are separated by the Shiina-Narashi out-of-sequence thrust fault (Figure 1B; Underwood et al. 1992). Based on vitrinite reflectance data, paleotemperatures of the Tertiary Shimanto Belt are estimated to be between 140°C and 315°C (Underwood et al. 1992, 1993b,c).

Paleotemperatures increase from north to south in the Murotohanto and the Nabae Groups (Underwood et al. 1992). In the Murotohanto Group, paleotemperatures are higher (215°C to 290°C) than in the Nabae Group (135°C to 285°C; Underwood et al. 1992). This is consistent with a post-metamorphic vertical offset of approximately 1,200 m (Underwood et al. 1992) across the Shiina-Narashi fault. Maximum pressures attained were not higher than 2.5 kbar (Underwood et al. 1992) representing burial depths of up to 9,000 m (Underwood et al. 1993b).

The rocks sampled in the Boso accretionary prism are taken as analogues for the deeper parts of the outer

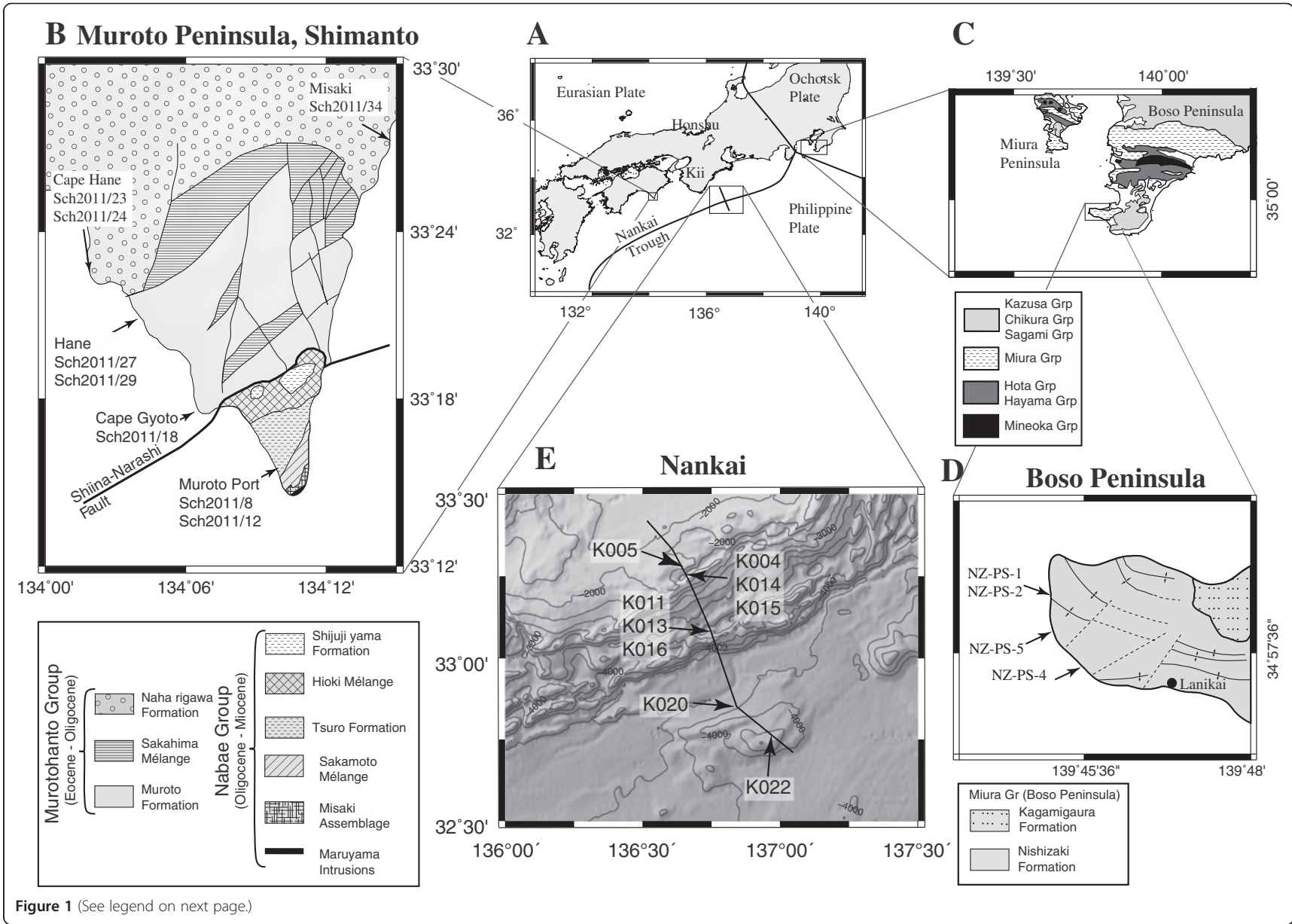


Figure 1 (See legend on next page.)

(See figure on previous page.)

**Figure 1 Study and sampling areas of tectonically exhumed accretionary complexes in central Japan.** (A) Map of central Japan. The position of the study areas are indicated by rectangular frames and shown in more detail in (B, C, E). (B) Geological map of the Muroto Peninsula, southern Shikoku Island (after Katto et al. 1991). (C) Map of the Tokyo Bay area showing the location of the Miura and Boso peninsulas (modified after Saito 1992 and Fujiwara et al. 1999). (D) Zoom in of the western Boso Peninsula headlands, showing the sample positions in the Nishizaki Formation (geological units according to Yamamoto et al. 2005). (E) Bathymetric map of the Nankai Trough area with indicated sample locations at IODP drill sites. Samples and IODP drill sites are related as follows: K005: Site C0001; K004, K014, K015: Site C0004; K013: Site C0006; K011, K016: Site C0007; K020: Site C0011; K022: Site 0012. The black line marks the Kumano transect taken for the IODP drilling campaign in the Nankai Trough (see Figure 2).

accretionary prism at Nankai (Figure 2). The Boso accretionary prism, of Miocene age, is located in central Japan and crops out on the Boso and Miura peninsulas (Figure 1C). Depositional ages range between 9.9 and 6.8 Ma (radiolarian biostratigraphy; Yamamoto and Kawakami 2005). The accretionary prism is formed by the Misaki Formation (Miura Peninsula) and the Nishizaki Formation (Boso Peninsula; Yamamoto 2006, Figure 1C). Since all samples were taken on the Boso Peninsula, we focus on the Nishizaki Formation, which forms the basal unit of the accretionary prism. It is unconformably overlain by trench slope cover sediments of the Kagamigaura Formation (Yamamoto et al. 2012) and by younger trench-fill sediments of the Chikura Group in the south of the Boso Peninsula (Kawakami and Shishikura 2006). The Nishizaki Formation is mainly made up of siltstones, with some scoriaceous sandstones and glassy tuffs (Yamamoto and Kawakami 2005). Maximum burial of the sediments is 1,000 m (Yamamoto et al. 2005), and there are ubiquitous deformation structures caused by tectonic accretion (Yamamoto et al. 2005). Vitrinite reflectance analyses indicate paleotemperatures below 50°C (Yamamoto et al. 2005). Because of the low degree of burial, high porosities between 30% and 50% are preserved (Yamamoto et al. 2005).

### Sample descriptions

Within the Murotohanto Group on Muroto Peninsula, the Naharigawa and Muroto Formations were sampled (Figure 1B; Table 1). As stated above, the Murotohanto Group has experienced paleotemperatures in the range of 215°C to 290°C. The Naharigawa Formation consists

of sandstones and shales, belonging to a sand-dominated turbidite sequence (Taira et al. 1982). Two mudstone outcrops were sampled, one approximately 750 m north of Cape Hane (west coast, samples Sch2011/23 and Sch2011/24; Figure 1B) and one in Misaki (east coast, sample Sch2011/34; Figure 1). At Cape Hane, black mudstones outcropping between massive sandstone of several meters of thickness were sampled (Sch2011/23 and Sch2011/24). At Misaki (Sch2011/34), no outcropping material could be sampled and loose mudstones had to be collected on the beach.

Shale-dominated turbidites with small amounts of tuff (Aitchison 1986), interpreted as melange complex (Taira et al. 1982), form the Muroto Formation. Olistostromal beds and extensive slumping structures were observed. Two suitable locations (Hane and Cape Gyoto; Figure 1B) on the west coast of Muroto Peninsula were sampled. The Hane samples (Sch2011/27 and Sch2011/29) come from a large outcrop of black mudstones approximately 1,000 m south of the mouth of the Hane River. The Cape Gyoto sample (Sch2011/18) comes from an outcrop directly southeast of the local fishing port.

The Nabae Group further south is made up of six lithological units. We sampled the Tsuru Formation near the southern tip of the Muroto Peninsula. It is made up of sandstone-shale assemblages (Hibbard et al. 1992; Underwood et al. 1993a) and olistostromal deposits (Aitchison 1986) and may be interpreted as a tectonic mélangé. Two mudstone samples were taken at the Muroto Port (Sch2011/8 and Sch2011/12; Figure 1B).

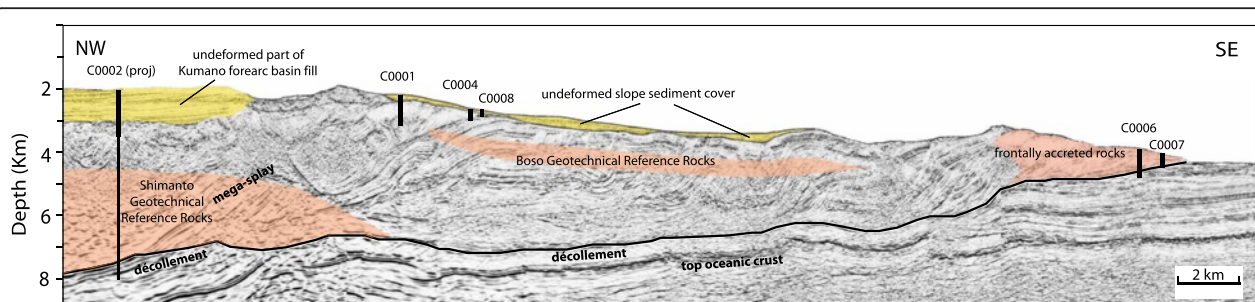


**Figure 2** Seismic section through the Nankai accretionary prism (Kumano transect; modified after Moore et al. 2009). The positions of rock units comparable to the tested Shimanto and Boso mudstones are shown. See text for discussion.

**Table 1 Sample locations and pressure and temperature conditions during burial**

Location	Sample	Latitude	Longitude	Pressure [kbar]	Burial depth [m]	Temperature [°C]
Cape Hane	Sch2011/23	33°22'38.1792"N	134°2'2.3136"E	2.5 (a)	9,000 (b)	215 to 230 (a)
	Sch2011/24					
Hane	Sch2011/27	33°21'38.8296"N	134°3'47.5236"E	2.5 (a)	9,000 (b)	270 to 290 (a)
	Sch2011/29					
Cape Gyoto	Sch2011/18	33°17'42.2124"N	134°7'1.5708"E	2.5 (a)	9,000 (b)	275 to 285 (a)
Muroto Port	Sch2011/8	33°16'31.3104"N	134°9'22.3164"E	2.5 (a)	7,800 (b)	190 to 225 (a)
	Sch2011/12					
Misaki	Sch2011/34	33°26'58.5528"N	134°14'26.6712"E		<1,000	<50 (c)
Sunosaki	NZ-PS-1	34°58'20.1864"N	139°45'12.9744"E		<1,000	<50 (c)
	NZ-PS-2					
	NZ-PS-5	34°57'57.2724"N	139°45'13.284"E		<1,000	<50 (c)
Nishikawana	NZ-PS-4	34°57'30.3012"N	139°45'50.67"E		<1,000	<50 (c)

Pressure and temperature conditions during burial according to (a) Underwood et al. (1993c), (b) Lewis et al. (2000), and (c) Yamamoto et al. (2005).

Four siltstone samples were collected on the Boso Peninsula. Samples NZ-PS-1, NZ-PS-2, and NZ-PS-5 come from the upper part, and sample NZ-PS-4 comes from the lower part of the Nishizaki Formation, which is part of the Miura Group (Figure 1C,D; Table 1). All sub-samples for triaxial testing were drilled normal to the sedimentary bedding. Sample NZ-PS-5 contains some angular clasts and some brighter patches, indicative for slumping of the unlithified sediment. Some darker gray oval-shaped patches of approximately 0.5 cm by 1 cm diameter, probably mud clasts resulting from sedimentary reworking, were observed at the sidewalls of the core sample.

## Methods

### Sample preparation

Because especially the mudstone samples from the Muroto Peninsula show strong foliation and resulting fissility, they required stabilization prior to coring. To achieve this, samples were embedded in high-viscosity epoxy resin (Epoxy4305 and resin hardener 'Härter1203-F', DD Composite GmbH, Bad Liebenwerda, Brandenburg, Germany), to provide a stable block for coring. Care was taken not to impregnate those parts that were chosen for coring and triaxial testing. After hardening of the epoxy resin, cores of 70-mm diameter were drilled perpendicular to the foliation. To achieve parallel end faces of the cylindrical samples, drill cores were cut and ground. Cutting the end faces also removed eventual epoxy resin. Thin caps of special dental gypsum ('Japan Stone') were added to the end faces of some samples to achieve ideal core lengths. Samples from the Boso Peninsula were drilled in the laboratory without the need for additional stabilization. The limited availability of the sample material precluded multiple tests. Prior to testing, cores were immersed in water for several hours to ensure ground moisture.

### Experimental setup

Specimens were tested using a computer-controlled triaxial apparatus at the geotechnical laboratory of the Institute of Geosciences at Martin-Luther-University Halle-Wittenberg (Germany). A 70-MPa pressure vessel capable of controlling the pore pressure and a hydraulic 5-MN loading device were used. Samples were jacketed in a 3-mm fiber-enhanced rubber tube to prevent contact with the confining medium (oil). Deformation experiments were carried out at room temperature at confining pressures ( $\sigma_3$ ) ranging between 25 and 65 MPa and pore pressures ranging between 25% and 90% of  $\sigma_3$ . Axial loading was with displacement rates of  $5.7 \times 10^{-6}$ /s (length normalized strain rate) until maximum differential stress of the pre-failure phase was reached. The elastic modulus (Young's modulus) was continuously computed from stress and strain gradients. Deformation was automatically stopped when the elastic modulus was constant or decreased when reaching the yield point. After this, pressure conditions were held constant for approximately 15 min. After the holding phase, the axial load was released slowly and the confining pressure was adjusted for the next deformation phase. This procedure was repeated up to five times for each sample. A detailed account of the experimental conditions during the different experiments is given in Table 2.

Three different types of triaxial tests were performed: (1) pore pressure stepping tests at variable pore pressure conditions. During the pore pressure stepping tests, the confining pressure ( $\sigma_3$ ) was held constant at 55 and 65 MPa, respectively. The pore pressure was decreased in three steps from 80% to 50% and 25% of the confining pressure or from 90% to 60% and 30% of the confining pressure, respectively. This allowed examining the peak strength at different effective confining pressure conditions. (2) In the

**Table 2 Experimental conditions of the triaxial tests presented in this study**

Sample	Experimental type	Confining pressure [MPa]	Pore pressure [% confining pressure]	Pore pressure [MPa]	Strain [%]	Peak stress [MPa]
Sch2011/23	CPST	25 - 35-45 - 55 - 65	80	20 - 28-36 - 44 - 52	1 - 1.25 - 1.49 - 1.8 - 2.1	94.6 - 110-120 - 132-136.5
Sch2011/24	PPST	55	80 - 50 - 25	44.0 - 27.5 - 14.0	1.8 - 2.4 - 3.4	126.4 - 157.7 - 184.3
Sch2011/34	PPST	65	90 - 60 - 30	58.0 - 39.0 - 19.5	0.48 - 1.4 - 3.8	105 - 139.5 - 186.4
Sch2011/27-2	PPST	55	80 - 50 - 25	44.0 - 27.5 - 14.0	1.4 - 2-2.7	173 - 156-173.7
Sch2011/27-1	CPST	25 - 35-45 - 55 - 65	80	20 - 28-36 - 44 - 52	0.2 - 0.4 - 0.78 - 1.2 - 1.6	102 - 115-131 - 142-155.8
Sch2011/29-2	CPST	25 - 35-45 - 55	80	20 - 28-36 - 44	0.8 - 1-1.1 - 1.2	120 - 104.3 - 123.6 - 141
Sch2011/18-2	PPST	55	90 - 60 - 30	49.5 - 33.0 - 16.5	0.4 - 3.4 - 4.7	240 - 248.8 - 246.7
Sch2011/8	CPST	25 - 35-45 - 55 - 65	80	20 - 28-36 - 44 - 52	0.4 - 0.6 - 1.2 - 1.7 - 2	172.7 - 157.8 - 141-150.6 - 155.6
Sch2011/12	PPST	55	90 - 60 - 30	49.5 - 33.0 - 16.5	0.4 - 2.3 - 4.7	96 - 157-223.7
NZ-PS-1/1	CPST	25 - 35-45 - 55 - 65	80	20 - 28-36 - 44 - 52	0.78 - 1-1.3 - 1.5 - 1.7	40.6 - 53.3 - 64.3 - 74.8 - 86
NZ-PS-1/2	PPST	55	90 - 60 - 30	49.5 - 33.0 - 16.5	0.8 - 1.9 - 2.7	76.1 - 74.3 - 73.3
NZ-PS-2	CPST	25 - 35-45 - 55 - 65	80	20 - 28-36 - 44 - 52	0.9 - 1.2 - 1.4 - 1.8 - 2	37.9 - 48.1 - 58.3 - 70.7 - 81.1
NZ-PS-4/1	CPST	25 - 35	80	20 - 28	1 - 1.2	55.8 - 66.1
NZ-PS-4/2	CPST	25 - 35	80	20 - 28	1.3 - 1.7	50.3 - 64.8
NZ-PS-5	CPST	25 - 35-45 - 55 - 65	80	20 - 28-36 - 44 - 52	0.6 - 0.8 - 1.0 - 1.2 - 1.4	41 - 53.4 - 62.6 - 75-87.2
NZ-PS-5-C	Cyclic test	55	80	44	0.9 to 1.17	69 to 70.2

In the confining pressure stepping tests (CPST), the confining pressure was increased in up to five steps, while in the pore pressure stepping tests (PPST), the pore pressure conditions were decreased in three steps. Confining and pore pressure conditions, achieved strains, and peak stresses are given for each step. Results of samples that failed during triaxial deformation experiments are given in italics. These values are not further considered.

confining pressure stepping tests, deformation tests were conducted at up to five different confining pressures. In these tests, the confining pressure was increased in each deformation phase in 10-MPa steps up to five times from 25 to 65 MPa, while the pore pressure was generally 80% of the confining pressure. Confining pressure stepping tests allow the determination of the peak strength at different confining pressure conditions of a sample. Deformation was stopped at the yield point in the pre-failure phase (Kovári and Tisa 1975) to avoid damage of the specimen and permit multiple tests. This procedure allows calculations of Mohr envelopes from the data to derive cohesion and angles of internal friction. Also, the influence of the variable pore pressure conditions can be studied in these tests. (3) A cyclic test (18 cycles) at constant confining pressure and constant pore pressure: In this test, confining pressure and pore pressure were kept constant ( $\sigma_3 = 55$  MPa, pore pressure =80% of  $\sigma_3$ ). The sample was cyclically loaded to a differential stress of 70 MPa. After the holding times, the axial load was decreased. This procedure was repeated 18 times. The cyclic test allows simulation of the effect of cyclic loading during earthquake cycles.

The study of samples from the Nankai accretionary wedge used for comparison used up to 100 mm long whole round core samples from IODP Expeditions 315, 316, and 333 for triaxial testing. The experimental procedures and conditions are given in Stipp et al. (2013), and the reader is referred to this paper. In brief, Stipp et al. (2013) conducted three types of tests: (1) single-step compression experiments, (2) pressure stepping experiments, and (3) displacement rate stepping experiments. Especially the confining pressure stepping tests are similar to the tests in this study, and in the 'Results' section below, we focus on these to enable direct comparison.

The effective shear parameter cohesion ( $C'$ ) and the angle of internal friction ( $\phi'$ ) were firstly determined from Mohr-Coulomb plots. Minimum requirements were three deformation stages; the results are given in Figure 3 and Table 3 and are described in the following paragraph. After plotting of the Mohr Circles, a tangent is fitted to the circles. The intersection of the tangent with the  $y$ -axis represents the cohesion of the samples, and the angle of the tangent directly reflects the angle of internal friction.

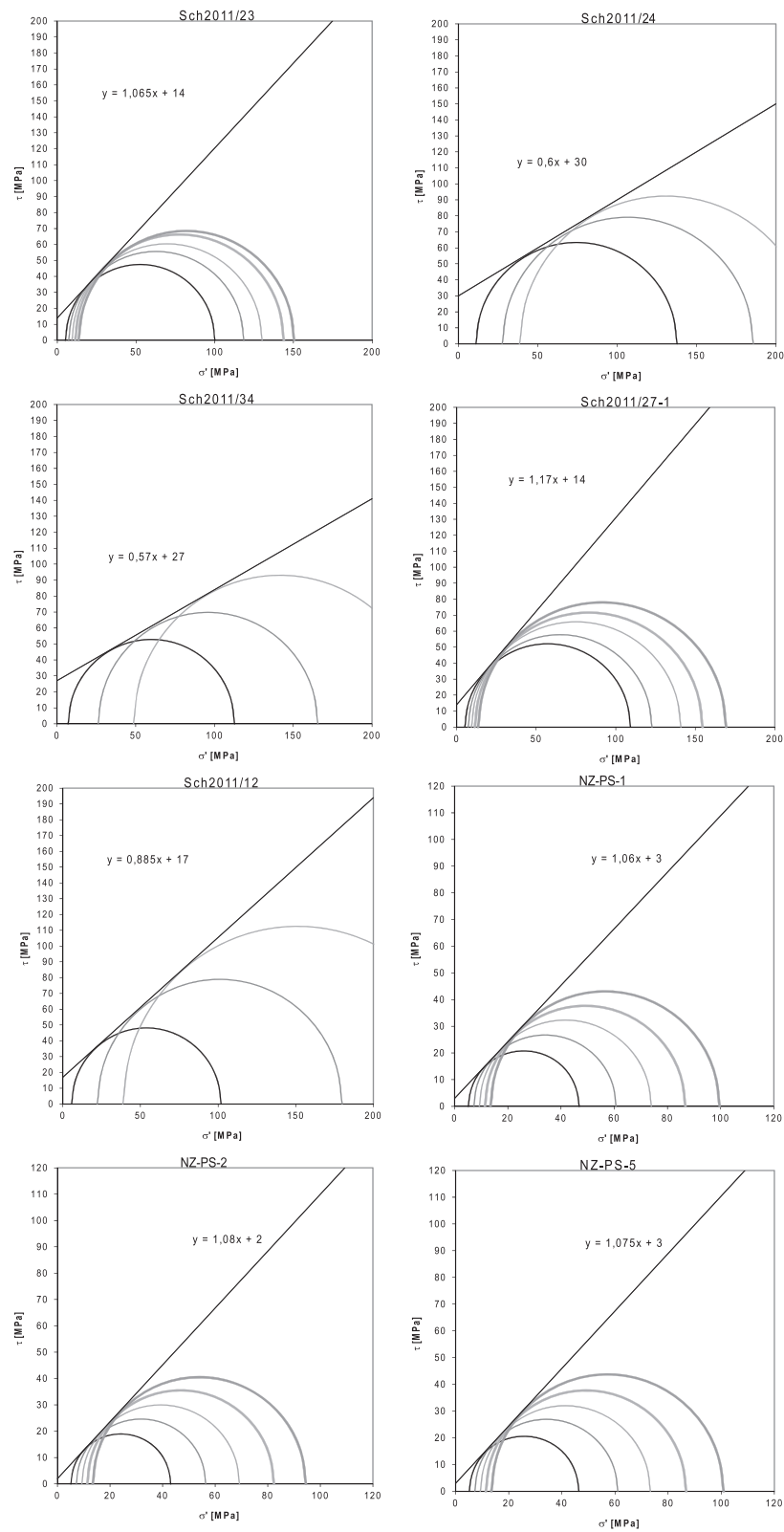


**Figure 3** Mohr Circle constructions to determine angles of internal friction and cohesion for eight of the tested samples.

**Table 3 Effective shear parameters determined from the triaxial tests**

Sample	Mohr-Coulomb		Stress path		Fracture angle	
	$\varphi$ [°]	C [MPa]	$\varphi'$ [°]	C' [MPa]	$\varphi_f$ [°]	C <sub>f</sub> [MPa]
Sch2011/23	46.8	14	45.15	15.4	47.6	12.8
Sch2011/24	30.96	30	33.44	30.04	21.8	42.3
Sch2011/34	29.68	27	30.83	25.18		
Sch2011/27-1	49.47	14	49.45	13.2	43.6	19.06
Sch2011/27-2					23.2	52.3
Sch2011/29-2					9	58.48
Sch2011/8					31.68	45.68
Sch2011/12	41.5	17	41.42	16.55	40	18.6
NZ-PS-1	46.66	3	46.68	2.89		
NZ-PS-2	47.07	2	46.28	2.31		
NZ-PS-4/1			45.64	6.14		
NZ-PS-4/2			50.9	2.65		
NZ-PS-5	47.07	3	47.14	2.62		
K004	27.1	0.0257				
K005	24.6	0.0249				
K011	35.8	0.0121				
K013	32	0.0293				
K014	28.7	0.0341				
K015	25.3	0.0497				
K016	40.4	0.0042				
K020	26.3	0.041				
K022	21.5	0.0354				

The Shimanto Belt samples (coded Sch2011) and the Boso accretionary prism samples (coded NZ-PS) were tested in this study, while the data from the Nankai samples (coded K) are taken from Stipp et al. (2013). Effective shear parameters were determined using Mohr-Coulomb criteria, stress path diagrams or fracture angle measurements.

Secondly, the effective shear parameters were determined from stress path constructions. For this, the maximum  $\sigma_1'$  and  $\sigma_3'$  of the deformation steps were plotted in a  $p'$ - $q'$  diagram (e.g., Burland 1990; Figure 4), where  $p'$  and  $q'$  are

$$p' = (\sigma_1' + \sigma_3')/2 \quad (1)$$

and

$$q' = (\sigma_1' - \sigma_3')/2 \quad (2)$$

According to Lang et al. (2003) and the German Industry Standard (DIN 18137 1990, part 2), the shear parameters  $C'$  and  $\varphi'$  can be calculated by plotting a regression line according to the following equations:

$$\varphi' = \arcsin(\tan \beta') \quad (3)$$

and

$$C' = b'/\cos \phi' \quad (4)$$

where  $\beta'$  is the angle of the regression line and  $b'$  is the intercept of the regression line with the  $y$ -axis.

Thirdly, the fracture angle  $\alpha$ , which is the angle between  $\sigma_1$  and the fracture (Figure 5; Additional file 1: Figure S2), can be used to derive effective shear parameters (e.g., Richter 1989; Twiss and Moores 1992). The double fracture angle is used to define the critical state of stress as shown in the Mohr Circle construction (Figure 5). The Coulomb criterion for fracture is defined by a tangent plotted from the intersection of the fracture angle plane and the Mohr Circle. From this, cohesion ( $C_f$ ) and the angle of internal friction ( $\varphi_f$ ) can be calculated. Since the samples from the Boso accretionary prism have not been fractured in the experiments, the effective shear parameters could only be determined for those Shimanto Belt samples that showed clear evidence for shear failure.

#### Analysis of sample composition

The mineralogical compositions of the Shimanto Belt samples were determined by synchrotron X-ray analysis using small drill cores of 2-cm diameter. Synchrotron X-ray measurements were conducted at the beam line W2 of HASY-LAB at the German Electron Synchrotron source (DESY), Hamburg. High-energy short-wavelength synchrotron radiation allows penetration of samples of several centimeters of thickness. In this way, intact samples can be measured without preparation. For further details on the measurement configuration and the data analysis, see Schumann et al. (2014) and Schumann (2014). Additionally, an X'Pert Pro X-ray diffractometer (X'Pert, PANalytical B.V., Almelo, The Netherlands) at the Department of Mineralogy at the Martin-Luther-University Halle-Wittenberg, Germany was used to analyze the composition of a sample from the Boso accretionary prism (NZ-PS-2). For this analysis, a powdered sample was measured from 5° to 70° 2-theta in steps of 0.016° 2-theta using Cu K $\alpha$  radiation.

## Results

### Sample composition

Compositions of the samples from the Shimanto Belt were determined by synchrotron X-ray-based Rietveld refinement (Rietveld 1969). For the composition analysis, small sample cylinders of 2-cm diameter were placed into the synchrotron X-ray beam. For further details on the processing steps, see Schumann et al. (2014) and Schumann (2014). Although samples of visually similar lithology were collected at the outcrops, some variability in sample compositions was found after evaluating the data (mineral contents are given in weight percent). The samples contain 30.5% to 51.5% quartz and 14.8% to 23.9% feldspar. Only sample Sch2011/18 shows higher feldspar content (32.3%). The lowest muscovite contents



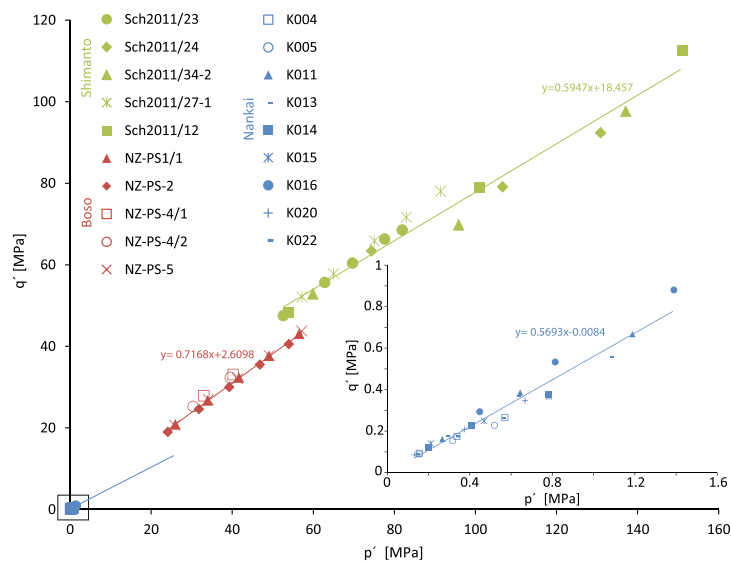


**Figure 4**  $p'$ - $q'$  plot determined from maximum  $\sigma_1$  and  $\sigma_3$  conditions achieved during triaxial testing in each deformation stage. Note that the Mohr-Coulomb slopes of each sample group are very similar. However, there are important differences in the cohesion, mainly reflecting different degrees of diagenesis or very low grade metamorphism in different settings. The qualities of fit ( $R^2$ ) for the three functions describing the Mohr-Coulomb slopes are as follows: Nankai: 0.9555, Boso: 0.9885, Shimanto: 0.9731. See text for discussion.

were found in the samples Sch2011/27 and Sch2011/29 with 8.5% and 6.5%, respectively. The other samples show muscovite contents of 10.7% to 16.4%. The total clay content ranges between 14.9% and 41.1%. A detailed overview of the compositions is given in Table 4.

The composition of the siltstones in the Boso samples was determined by X-ray powder diffraction (Kameda et al. 2010). For details on the sample treatment and analyzing steps, see Kameda et al. (2010). Samples NZ-PS-1 and NZ-PS-2 are taken from a place close to Sample SU23. Sample NZ-PS-4 is identical with NK26, and sample NZ-PS-5 is identical with NK24 of Kameda et al. (2010). According to Kameda et al. (2010), the sediments consist of quartz (30%), illite (10% to 20%), plagioclase (10%), kaolinite + chlorite (5%), and calcite (0% to 10%). The composition of sample NZ-PS-2 was determined in this study by quantitative X-ray powder diffraction (XRD) analysis. Contents are 20.1% quartz, 32.9% plagioclase, 3.9% calcite, 22.9% clay, 4.7% muscovite, and 10.5% chlorite (Table 4). Besides the additional phases found in our analysis, the composition is similar to the compositions found by Kameda et al. (2010).

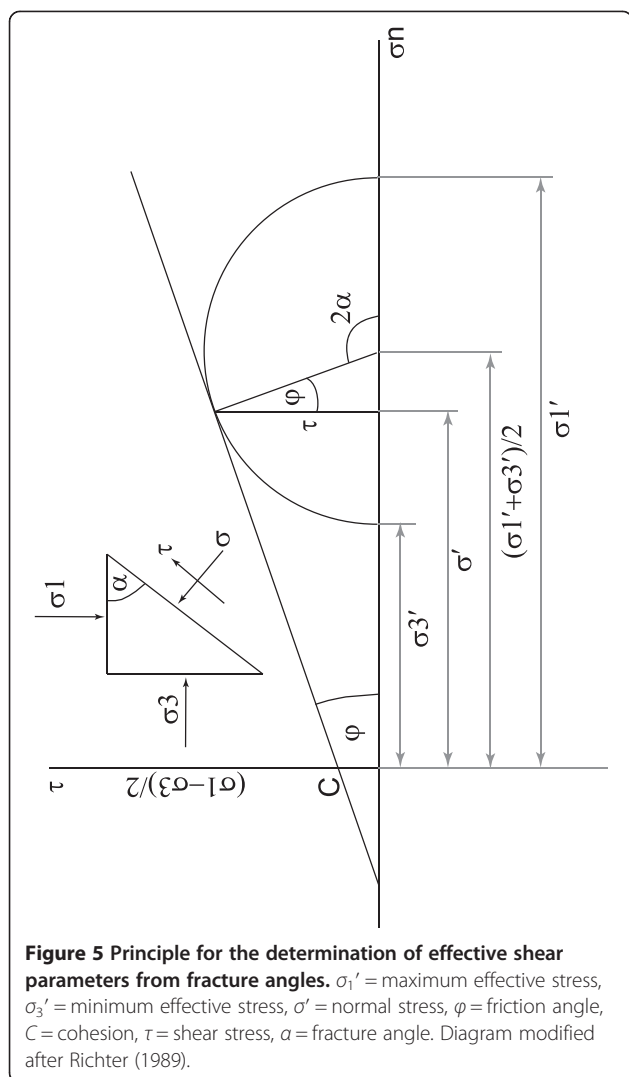
#### Effective shear parameters

Detailed descriptions of the experimental results are given in the Additional file 1 of this paper. For the Shimanto Belt samples Sch2011/12, Sch2011/23, Sch2011/24, Sch2011/27-1, and Sch2011/34 (Additional file 1: Figures S1 and S3) and for the Boso samples NZ-PS-1, NZ-PS-2, and NZ-PS-5 (Additional file 1: Figure S4), maximum  $\sigma_1$  and  $\sigma_3$  could be determined for at least three deformation stages, and the

corresponding Mohr-Coulomb envelopes could be plotted (Figure 3; Table 3). Samples Sch2011/8, Sch2011/18, Sch2011/27-2, and Sch2011/29 showed failure after the first deformation stage (Additional file 1: Figures S1 and S3), and therefore, no corresponding computation of Mohr-Coulomb envelopes was possible. Samples NZ-PS-4/1 and NZ-PS-4/2 were tested in only two pressure steps (Additional file 1: Figure S4), and Mohr-Coulomb envelopes were not computed. The values for cohesion of the Shimanto Belt samples range between 14 and 30 MPa, and for the samples from Boso, the range is between 2 and 3 MPa. Angles of internal friction range between 29° and 49° and between 41° and 47° for the Shimanto Belt and Boso samples, respectively.

Secondly, cohesions could be determined from stress path constructions. For the Shimanto Belt samples, values are between 13 and 30 MPa and between 2.3 and 6.14 MPa for the Boso samples. Angles of internal friction determined by this method range between 33.4° and 49.5° and between 45° and 50° for the Shimanto Belt and Boso samples, respectively (Table 3).

In a third approach, we determined the effective shear parameters from fracture angles (see above). Since samples from the Boso accretionary prism did not mesoscopically fracture in the experiments, the effective shear parameters were only determined for those Shimanto Belt samples that showed clear evidence for shear failure. Cohesion values determined using this method are slightly higher (between 18.6 and 42.3 MPa) than the values determined by Mohr Circle constructions or stress path diagrams, except for sample Sch2011/23, which has a lower cohesion



of 12.8 MPa. Angles of internal friction are generally lower (between 21.8° and 43.6°) except for sample Sch2011/23, which has a higher angle of internal friction compared to the other methods (Table 4). Sample Sch2011/29 has a very low angle of internal friction of 9°. Especially for those samples that failed in the first deformation phase (samples Sch2011/8, Sch2011/18, Sch2011/27-2, and Sch2011/29; see Additional file 1: Figures S1 and S3), the method is helpful in constraining the effective shear parameters, as they could not be determined by the other two methods.

## Discussion

### Effective shear parameters

The effective shear parameters were determined using Mohr Circle constructions, stress path constructions ( $p'$ - $q'$  diagram), and estimations from fracture angles. The first two methods use the same experimental values (Figures 3 and 4; Table 3). Differences in the effective shear parameters determined by these methods are small (Table 3) and

may result from the different fit of the tangent to the Mohr Circles and the fit of the regression line to the stress maxima. Shear parameters determined from the fracture angles on the same samples differ to a slightly larger extent. Since we conducted up to five experimental steps using single samples (see the 'Methods' section), maximum shear stresses at the moment of failure cannot be exactly determined; thus, any results from the computations have to be considered as close approximations of the real values. The fracture angle method, on the other hand, is more prone to measurement errors, and fracture angles in some cases have irregular geometries and show multiple fracturing (see, e.g., Additional file 1: Figure S2B). One further effect on fracture angles may be exercised by sample length. Additional file 1: Figure S2B shows that dimensions of the sample cylinders are just sufficient to ensure pervasive shear failure of the samples, so that boundary effects cannot be ruled out completely. Unfortunately, it was impossible to produce samples for the testing with length-diameter ratios much larger than 2, which is desirable for triaxial testing. As a result, fracture angles (Figure 5) may be somewhat lower than in experiments with unconstrained sample length, leading to an underestimation of angles of internal friction and overestimation of cohesion. This is reflected in the results for most samples (compare values in Table 3). Finally, fracture angles may also be influenced by fabric anisotropy, such as the preferred alignment of sheet silicates, and reactivation of pre-existing microfractures and joints. This, however, is an effect that should be equally evident in the results of shear parameter computations, as anisotropy is an intrinsic property that influences rock friction and the energetics of fracture formation.

### Comparison with studies of related rocks

The high internal friction angles derived for the Shimanto and Boso siltstone samples studied here show that the response to pre-failure loading is similar to that of hard rocks (see, e.g., discussion in Savage et al. 1997) and describes a mechanical state preceding the development of coalescing microcracks to produce failure. Studies of Hajdarwish and Shakoor (2006) and Lempp et al. (2010) determined the effective shear parameters for claystone, mudstone, siltstone, shale, and slate. Hajdarwish and Shakoor (2006) report cohesion values between 0.24 and 7.84 MPa and angles of internal friction range between 10.9° and 35.8°. Sediments from shallow marine settings of depths between 1,000 and 2,100 m investigated by Lempp et al. (2010) show cohesion between 1 and 6 MPa for mudstones, between 2 and 7 MPa for shales, and between 10 and 20 MPa for more lithified slates (Lempp et al. 2010). The angle of internal friction ranges between 15° and 25° for mudstone and shale, and between 20° and 30° for the slates (Lempp et al. 2010). The higher

**Table 4 Mineralogical compositions of the three sample subsets**

	Sample	Quartz	Feldspar	Calcite	Muscovite	Total clay	Clay + mica	Qtz + fsp	Reference
Boso	NZ-PS-1	27	15	3		54	54	42	Kameda et al. (2010) This study
	NZ-PS-2	28	15	3		54	54	42	
	NZ-PS-2	20.1	32.9	3.9	4.7	38.1	42.8	53	
	NZ-PS-4	28	10	6		56	56	38	
	NZ-PS-5	31	9	0		60	60	40	
Shimanto Belt	Sch2011/23	41.8	19.9		14.7	23.2	37.9	61.7	This study
	Sch2011/24	30.5	17.5		10.7	41.1	51.8	48.0	
	Sch2011/27	51.6	17.8		8.58	21.8	30.3	69.4	
	Sch2011/29	42.1	19.8		6.2	31.5	37.7	61.9	
	Sch2011/18	35.0	32.3		13.2	19.2	32.4	67.3	
	Sch2011/34	38.8	21.9		16.4	22.7	39.1	60.7	
	Sch2011/8	46.0	23.9		14.7	14.9	29.6	70.8	
	Sch2011/12	36.5	14.8		12.7	35.7	48.4	51.3	
Nankai	K004	39.2	20.1	14.1		39.2		59.3	Schumann et al. (2014)
	K005	20.6	12.9	16.8		49.4		33.5	
	K011	No data							
	K013	No data							
	K014	31.2	25.6	6.6		36.3		56.8	
	K015	34.7	25.6	5.1		34.4		60.3	
	K016	38.1	31.8	0.1		29.7		69.9	
	K020	No data							
	K022	28.3	29.8	6.6		35.1		58.1	

The composition of sample NZ-PS-2 was determined by X-ray powder diffraction (XRD) in this study. The composition of the samples from the Shimanto Belt and from Nankai was determined by synchrotron X-ray diffraction-based Rietveld refinement (Rietveld 1969). Mineral contents are given in weight percent. qtz, quartz; fsp, feldspar; mica, muscovite.

level for cohesion and angle of friction found in the Shimanto Belt siltstones (see compositions in Table 3) indicate that the deep burial (between 7,800 and 9,000 m) went along with strong diagenesis (e.g., Kimura et al. 2007) and very low grade metamorphism at zeolite to prehnite-pumpellyite facies (DiTullio and Byrne 1990; Banno and Nakajima 1991) resulting in the formation of tough, strongly anisotropic, low-porosity rocks. More siliceous sedimentary rocks, similar to the Boso samples regarding depth of burial and absence of diagenetic overprint, were investigated by Roller et al. (2003) from the Tohoku forearc further north along the Japan margin. Samples are from the Ocean Drilling Program (ODP) Sites 1150 and 1151, two drill holes in the forearc slope cover. Cohesion values from depths similar to the Boso setting (between 864 and 1,101 mbsf) range between 0.16 and 2.3 MPa. The cohesion of the Boso samples is in a similar range except for sample NZ-PS-4/1, which has a higher cohesion (6.14 MPa; Table 4). Angles of internal friction of the Boso samples are somewhat higher than those from the Nankai or the Shimanto Belt (Table 3). Friction angles of sample materials from ODP drilling along the Muroto transect presented by Ask and Morgan

(2010) of approximately 40° and approximately 44° are slightly lower than the data determined for the Boso samples, but higher than those in most samples tested from the Nankai accretionary prism (Stipp et al. 2013; Table 3 of this study) and the Shimanto Belt (Table 3). High internal friction angles might be a result of the sample composition. Differences in the sample compositions can be found comparing the data presented in Table 4. Although differences in the quartz + feldspar and clay + mica content of the Shimanto and Boso samples do exist, no clear relation of the sample composition to high angles of internal friction can be found in our data (compare Tables 3 and 4). For example, the angle of internal friction in sample Sch2011/24, which shows approximately similar values of quartz + feldspar and clay + mica compared to the Boso samples, is lower than that in the Boso sample set. On the other hand, in sample Sch2011/23, the quartz + feldspar content is much higher compared to that in the Boso sample set and the clay + mica content is much lower, but the observed internal friction angles in both samples are approximately similar. For this reason, a clear correlation of the sample composition to high or low internal friction angles is not obvious. Therefore, we may suspect that the

reason for the high angles of internal friction may lie in the microfabric of the Boso rocks. This, however, is beyond the scope of this study.

When all available data from this study and the data of Stipp et al. 2013 are plotted in a summary  $p'$ - $q'$  diagram (Figure 4), it is immediately obvious that the fits within the individual sample subsets (Nankai, Boso, Shimanto) are quite good, with only small scattering.  $R^2$  values for the fit are 0.9555 (Nankai), 0.9885 (Boso), and 0.9731 (Shimanto). There is very little variation of slopes describing the relation of effective mean stress ( $p'$ ) and shear stress ( $q'$ ) between the three data sets. However, at the transition (around 50 to 60 MPa) between the Shimanto and the Boso subsets, the Shimanto subset shows an about 8 MPa higher value for  $q'$  than the Boso subset, where the effective mean stress overlaps. We interpret this as being caused by diagenetic changes, cementation and compaction, that have affected the deeply buried Shimanto sample subset. The temperature and pressure conditions of the Shimanto samples indicate zeolite to prehnite-pumpellyite facies (e.g., Hashimoto et al. 1970; Toriumi and Teruya 1988; DiTullio and Byrne 1990; Banno and Nakajima 1991), and the documented range of paleotemperatures for the formations sampled is 215°C to 290°C (Underwood et al. 1992). The 8-MPa difference in cohesion, therefore, reflects this diagenetic and/or metamorphic change. When linearly extrapolating the Nankai data set shown in Figure 4 to  $p'$  of 25 MPa, there is a smaller jump of about 3 MPa in values for  $q'$  between the Boso and Nankai subsets. This likely relates to the higher effective stresses (e.g., Ikari and Kopf 2011) the Boso rocks have undergone during burial, compaction, and tectonic deformation, without having been subjected to significant cementation, however (Yamamoto et al. 2005). The paleotemperatures have probably not exceeded 50°C for the Boso samples (Yamamoto et al. 2005), too low to induce any substantial mineralogical change. The samples of the Nankai subset come from the upper 120 m below the sea floor and suffered relatively minor compaction in response to burial and tectonic overprint, which is reflected by very low cohesion.

#### Significance of the cyclic test

Decreasing axial strains at the beginning of the cyclic test on sample NZ-PS-5-c are attributed to settlement of the sample material due to the applied load. The increasing axial strains after this phase of settlement (cycles 5 to 18; Figure 6) are interpreted to reflect small amounts of irreversible creep in the sample material in each experimental cycle. The total amount of creep accumulated in cycles 5 to 18, however, is smaller than the amount of initial deformation due to pressurization. If this behavior is typical for the Boso rocks, it can be inferred that they seem to be prone to creep rather than to brittle deformation during earthquake shaking. This

would be in accordance with the rather low cohesion of the samples and is supported by the observation that the drill cores after triaxial deformation did not show throughgoing fractures. Low degrees of compaction, relatively high porosities, and the absence of cementation (Yamamoto et al. 2005), as discussed above, support this interpretation.

#### Tectonophysical implications for the Nankai forearc and accretionary wedge

Following the line of reasoning developed above, the observations on rock strength and effective shear parameters in the three sample subsets can in principle be used to make some predictions of the mechanical behavior of the Nankai accretionary prism and its décollement zone at depth. Figure 7 shows the range of variation in cohesion to be expected to a depth of 9,000 mbsf, supposing that the prism and underlying units are dominantly composed of mudstones and siltstones with mechanical behavior analogous to the Boso and Shimanto samples. The results from the testing of the Shimanto subset constrain a substantial amount of cohesion, between about 13 and 30 MPa for 9,000-m depth. If we consider the geometry of the Nankai accretionary wedge and forearc in the Kumano transect (Figure 2), it is evident that the rock suite overlying the basal décollement below the Kumano forearc basin is approximately 5,500 m thick at IODP Site C0002, where the plate boundary fault is to be drilled, cored, and instrumented. The strata of the forearc basin are undeformed, which means that the accreted rocks underneath must be cohesive enough to resist deformation, and constitute a stronger basal inner prism akin to the conceptual model in Figure 8, with cohesions of about 8 to 18 MPa (Figure 7). On the other hand, the rocks in the décollement itself should be less cohesive at this depth according to the Coulomb wedge theory, to assure concentration of the full rate of long-term interplate movement there. Presently, the décollement at the updip end of the seismogenic zone beneath the Kumano Basin is locked, which provides evidence that it is relatively stronger than the bounding zones (Saffer and Tobin 2011). Similarly, interplate movement in the strong outer prism area is concentrated in the underlying décollement (see Figure 8), with the exception that most interplate movement here probably occurs aseismically. At about 1,000-m depth beneath the cover, the accreted rocks must be at least as cohesive as the rocks that were tested from Boso, i.e., 2 to 3 MPa. Above the level of the décollement, approximately 3,000 to 4,000 mbsf, the rocks would be expected to have cohesions in the range of 5 to 12 MPa (Figure 7) and be floored by a weaker plate boundary fault. At the toe of the outer prism weak, almost cohesionless and unlithified rocks overlie a weak décollement. The fact that cohesions in the décollement at the toe of the outer prism

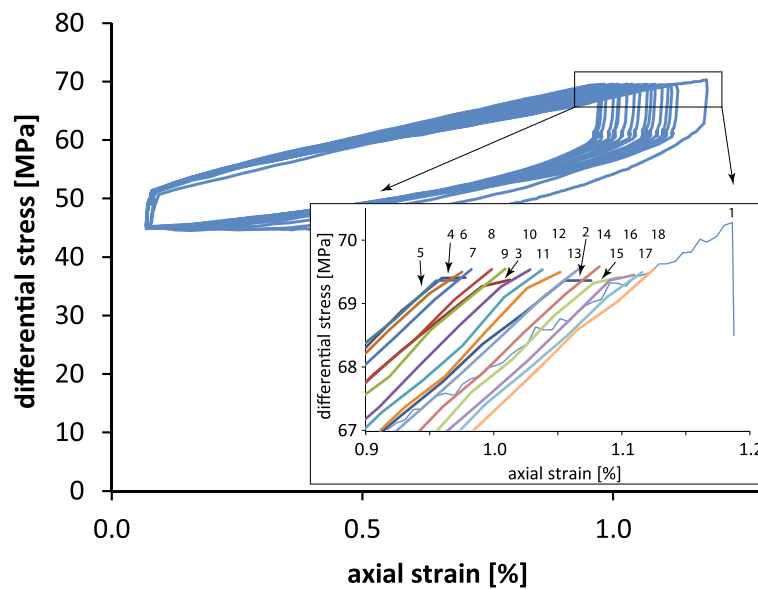
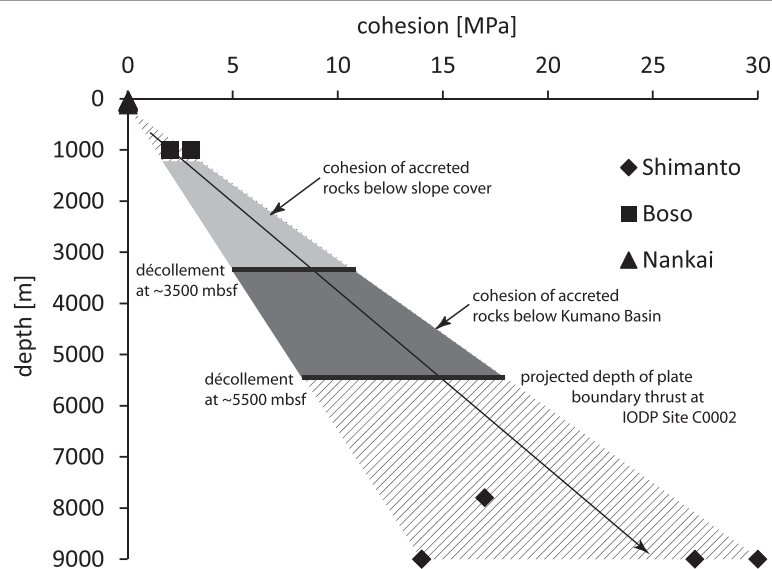


**Figure 6** Cyclic deformation experiment of sample NZ-PS-5-c. The sample was axially loaded 18 times to a differential stress of approximately 70 MPa at 55-MPa confining pressure and 44-MPa pore pressure. The inset shows the records of strain accumulation during the individual loading cycles labeled 1 to 18.

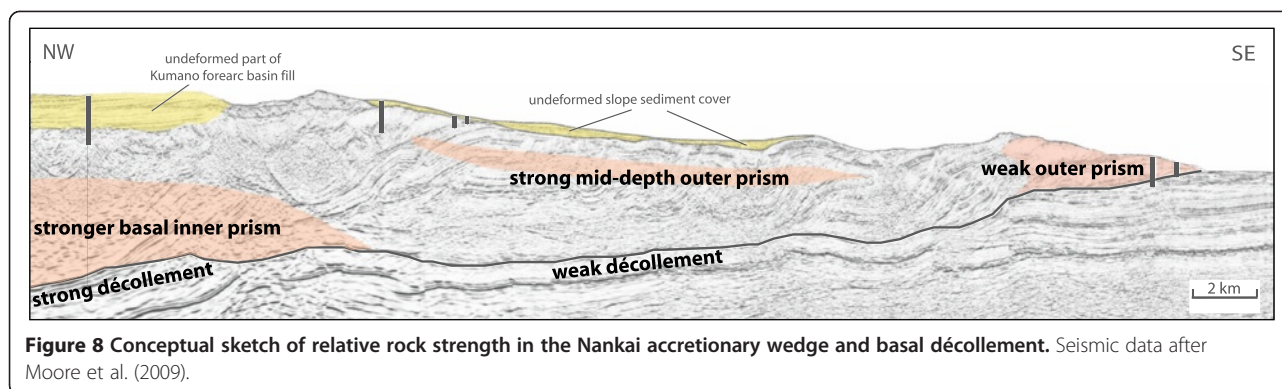
(Figure 8) cannot differ substantially from the rocks above results in distributed strain in the wedge and frontal imbrication.

Figure 4 shows that the frictional behavior of all three subsets of rocks approximates Coulomb-type laws (e.g., Dahlen 1990; Marone et al. 1992) and is probably very similar, with estimated angles of static friction of about 30° (Nankai, Shimanto) and 35° (Boso). The slopes of the  $p'$ - $q'$  functions imply static friction coefficients of

about 0.57 (Nankai), 0.59 (Shimanto), and 0.72 (Boso). These values are compatible with those measured from a wide range of fault gouges, especially those containing significant amounts of quartz and feldspar in addition to clay minerals such as kaolinite and illite (see, e.g., Ikari et al. 2011 for a compilation). Smectite, which is present in significant amounts in the mudstones from Nankai (e.g., Underwood 2007; Guo and Underwood 2012; Stipp et al. 2013) and Boso (see Table 3), is thought



**Figure 7** Plot of cohesion versus depth of burial for the three sample sets. The different data sets are used to extrapolate the cohesion of the sedimentary rocks beneath the slope cover and down to the updip end of the seismogenic zone in the active Nankai subduction zone. See text for discussion.



to change frictional properties towards lower values (e.g., Logan and Rauenzahn 1987). However, the similar frictional properties of all three subsets would argue against the importance of such effects. The cohesions that can be derived from linear regressions of the data from the three subsets of samples (Figure 4) are about 8 kPa for Nankai, about 2.6 MPa for Boso, and about 18.5 MPa for the Shimanto Belt. Again, this illustrates how important diagenesis (e.g., Kimura et al. 2007), cementation, and very low grade transformations are defining the strength of forearc rocks.

In summary, it appears that the hydrological properties of the décollement and the accreted rocks (Morgan and Karig 1995; Skarbek and Saffer 2009) at Nankai and geomechanical effects like structural strength or weakness (Stipp et al. 2013) are very important controlling variables, determining strain localization and fault propagation. Compositional variations are possibly too subtle to constrain differences in frictional behavior. They have also been found to be of only very little importance in the Nankai sample set (see Stipp et al. 2013). Burial-dependent increases in cohesion, resulting from diagenesis and, at greater depths, from very low-grade metamorphism, are probably of overriding importance in determining rock strength in the accretionary wedge and forearc. If the data presented in this study from the Boso and Shimanto belts are taken as analogues, then the prism is strong enough to transmit stresses as high as 5 to 13 MPa to the frontal 10 km (Figure 8). The locked updip end of the seismogenic zone below IODP Site C0002 can probably support stresses up to 18 MPa without rupturing, if it is supposed that the fault zone is healed and recemented during the interseismic cycle.

## Conclusions

The results of triaxial shear tests on mudstone samples from the Shimanto Belt and the Boso accretionary prism (Japan) allowed an assessment of the strength evolution

of terrigenous to hemipelagic active margin sediments with progressive burial and diagenesis. Effective shear parameters were derived from suites of triaxial pressure stepping tests at increasing confining pressures. A cyclic loading test on one sample from Boso (18 cycles to 70-MPa differential stress) showed that after some contraction due to pressurization in the first five cycles, the sample had tendencies to creep at constant stress rather than to fracture at maximum applied load. This may be typical for the Boso mudstones tested, as the other cores were also not fractured during the experiments. The samples from the Shimanto Belt, in turn, showed evidence of dominantly brittle behavior during testing. In both sample subsets effective shear parameters indicate that the phyllosilicate-quartz-feldspar mudstones are relatively strong sediments. Internal angles of friction are partly quite high. Cohesion is in the range of 2 to 6 MPa for the Boso samples and between 13 and >30 MPa for those from the Shimanto Belt. Because the compositions of both sample subsets are similar to those of mudstones from the recently active Nankai accretionary prism and forearc, the results can be used to make some predictions about the strength and frictional behavior of the deeper parts of the Nankai active margin and the décollement at its base. Static friction is similar to results in the literature, obtained from tests on a wide range of phyllosilicate-quartz-feldspar gouges. Cohesion increase due to diagenesis and/or very low grade metamorphism is of overriding importance in determining the strength of the deeper parts of the forearc. Judging from the increase of cohesion with depth, pre-fracture stresses of up to 18 MPa may be transmitted through the updip end of the seismogenic zone at depth at Nankai and about 5 to 13 MPa through the backstop of the actively deforming frontal prism. As the rocks above the updip end of the seismogenic zone and above the mid-slope part of the accretionary wedge are not deforming at present, it is inferred that cohesion of fault rocks in the décollement is lower than the values given above.

## Additional file

**Additional file 1: Figure S1.** Stress–strain plots of the confining pressure stepping tests of the Shimanto Belt samples. **Figure S2.** Examples of drill cores after triaxial testing. **Figure S3.** Stress–strain plots of the pore pressure stepping tests conducted on the Shimanto Belt samples. **Figure S4.** Stress–strain plots of the confining pressure stepping tests of the Boso samples.

## Competing interests

The authors declare that they have no competing interests.

## Authors' contributions

KS conducted the field work in the Shimanto Belt in collaboration with YK, JHB, and MS. KS also prepared and described related core samples, participated in the triaxial testing, interpreted the experimental results and drafted the manuscript. JHB and MS supervised KS, and contributed to the data interpretation and writing. YY carried out the field work in the Boso paleo-accretionary prism and provided core samples. CL conducted the triaxial tests on the Shimanto and Boso samples and helped in the data interpretation. All authors contributed to various topics of discussion and agreed in the final manuscript.

## Acknowledgements

The authors sincerely thank Y. Hashimoto and W. Lin for the logistical help and guidance during the fieldwork. We are grateful to the laboratory staff at Martin-Luther-University Halle-Wittenberg and to R. Kaden for the XRD measurements. We thank the editor M. Kinoshita and two anonymous reviewers for their thoughtful comments and suggestions, which greatly helped to improve the manuscript. JHB and MS acknowledge the funding of this work by Deutsche Forschungsgemeinschaft (DFG) Grant BE1041/28.

## Author details

<sup>1</sup>Marine Geodynamics, GEOMAR Helmholtz Centre for Ocean Research Kiel, Wischhofstr. 1-3, Kiel, Germany. <sup>2</sup>IFREE, JAMSTEC, 3173-25 Showa-machi, Kanazawa-ku, Yokohama 236-0001, Japan. <sup>3</sup>Department of Earth and Environmental Sciences, Graduate School of Science and Engineering, Kagoshima University, 1-21-35 Korimoto, Kagoshima 890-0065, Japan. <sup>4</sup>Institut für Geowissenschaften und Geographie, Martin-Luther-Universität Halle-Wittenberg, Von-Seckendorff-Platz 3, 06120 Halle (Saale), Germany.

Received: 22 November 2013 Accepted: 17 September 2014

Published: 16 October 2014

## References

- Aitchison J (1986) Stratigraphy, sedimentology and tectonic evolution of the Shimanto Terrane, Southwest Japan. *Earth Science; Journal of the Association for the Geological Collaboration in Japan* 40:337–363
- Ask MVS, Morgan JK (2010) Projection of mechanical properties from shallow to greater depths seaward of the Nankai accretionary prism. *Tectonophysics* 482:50–64, doi:10.1016/j.tecto.2009.08.023
- Banno S, Nakajima T (1991) Metamorphic belts of Japan. *Episodes* 14:280–285
- Brace WF, Byerlee JD (1966) Stick-slip as a mechanism for earthquakes. *Science* 153:990–992
- Burland JB (1990) On the compressibility and shear strength of natural clays. *Geotechnique* 40:329–378
- Byrne DE, Davis DM, Sykes LR (1988) Loci and maximum size of thrust earthquakes and the mechanics of the shallow region of subduction zones. *Tectonics* 7:833–857
- Dahlen FA (1990) Critical taper model of fold-and-thrust belts and accretionary wedges. *Annu Rev Earth Planet Sci* 18:55–99
- DIN 18137 (1990) Testing procedures and apparatus: triaxial test, part 2 (German Industry Standard). Deutsches Institut für Normung, Berlin
- DiTullio L, Byrne T (1990) Deformation paths in the shallow levels of an accretionary prism: the Eocene Shimanto belt of southwest Japan. *Geol Soc Am Bull* 102:1420–1438, doi:10.1130/0016-7606(1990)102<1420:DPITSL>2.3.CO;2
- DiTullio L, Hada S (1993) Regional and local variations in the thermal history of the Shimanto Belt, southwest Japan. In: Underwood MB (ed) *Thermal evolution of the tertiary Shimanto belt, southwest Japan: an example of ridge-trench interaction*. Geological Society of America, special paper 273
- Fujiwara T, Kinoshita H, Morijiri R (1999) Magnetic structure of the southern Boso Peninsula, Honshu, Japan, and its implications for the formation of the Mineoka Ophiolite Belt. *JAMSTEC Earth Planets and Space* 51:413–424
- Guo J, Underwood MB (2012) Data report: clay mineral assemblages from the Nankai trough and Kumano basin, IODP expedition 315 and 316, NanTroSEIZE stage 1. In: Kinoshita M, Tobin H, Ashi J, Kimura G, Lallemand S, Screation EJ, Curewitz D, Masago H, Moe KT and the Expedition 314/315/316 Scientists, *Proc. IODP, 314/315/316*, doi:10.2204/iodp.proc.314315316.202.2012
- Hajdarwish A, Shakoor A (2006) Predicting the shear strength parameters of mudrocks. The Geological Society of London, IAEG2006, paper number 607
- Hashimoto M, Igi S, Seki Y, Banno S, Kojima G (1970) Metamorphic facies map of Japan. Geological Survey of Japan, Kawasaki
- Hibbard J, Karig D, Taira A (1992) Anomalous structural evolution of the Shimanto accretionary prism at Murotomisaki, Shikoku Island, Japan. *Island Arc* 1:133–147
- Hyndman RD, Wang K (1993) Thermal constraints on the zone of major thrust earthquake failure – the Cascadia subduction zone. *J Geophys Res* 98:2039–2060
- Hyndman RY, Wang K, Yamano M (1995) Thermal constraints on the seismogenic portion of the southwestern Japan subduction thrust. *J Geophys Res* 100:15373–15392
- Ikari MJ, Kopf AJ (2011) Cohesive strength of clay-rich sediment. *Geophys Res Lett* 38, doi:10.1029/2011GL047918
- Ikari MJ, Marone C, Saffer DM (2011) On the relation between fault strength and frictional stability. *Geology* 39:83–86, doi:10.1130/G31416.1
- Kameda J, Yamamoto Y, Kimura G (2010) Smectite swelling in the Miura-Boso accretionary prism: possible cause for incipient décollement zone formation. *Tectonophysics* 494:75–84, doi:10.1016/j.tecto.2010.08.008
- Katto J, Hada M, Tashiro M, Taira A, Terado T (1991) Geological and mineral spring resources map of Kochi Prefecture. Kochi Prefecture Government, Kochi
- Kawabata K, Tanaka H, Kimura G (2007) Mass transfer and pressure solution in deformed shale of accretionary complex: examples from the Shimanto Belt, southwestern Japan. *J Struct Geol* 29:697–711
- Kawakami S, Shishikura M (2006) Geology of the Tateyama District, quadrangle series, 1:50,000. Geological Survey of Japan, AIST, Tokyo, p 82, in Japanese with English abstract
- Kimura G, Ludden J (1995) Peeling oceanic crust in subduction zones. *Geology* 23:217–220
- Kimura G, Kitamura Y, Hashimoto Y, Yamaguchi A, Shibata T, Ujiie K, Okamoto S (2007) Transition of accretionary wedge structures around the up-dip limit of the seismogenic subduction zone. *Earth Planet Sci Lett* 255:471–484
- Kovári K, Tisa A (1975) Multiple failure state and strain controlled triaxial tests. *Rock Mech* 7:17–33
- Kumon F (1983) Coarse clastic rocks of the Shimanto Supergroup in eastern Shikoku and Kii Peninsula, southwest Japan. *Memories of the Faculty of Science, Kyoto University, Series of Geology and Mineralogy* 49:63–109
- Kuramoto S, Curewitz D, Thu MK, Masago H, and the Expedition 314, 315 and 316 Science Parties (2008) The first D/V Chikyu IODP operations: successful logging and coring during NanTroSEIZE stage 1 expeditions. *Sci Drill* 6:38–42, doi:10.2204/iodp.sd.6.05.2008
- Lang HJ, Huder J, Amann P (2003) *Bodenmechanik und Grundbau*, 7th edn. Springer, Berlin
- Lempp C, Witthaus M, Roedel T, Hecht K, Herold M (2010) Geomechanisches Verhalten diagenetisch unterschiedlich stark verfestigter pelitischer Gesteine in tiefen Geothermiebohrungen. *Z Dtsch Ges Geowiss* 161(4):379–400, doi:10.1127/1860-1804/2010/0161-0379
- Lewis JC, Byrne TB, Pasteris JD, London D, Morgan GB (2000) Early tertiary fluid flow and pressure-temperature conditions in the Shimanto accretionary complex of south-west Japan: constraints from fluid inclusions. *J Metamorph Geol* 18:319–333
- Logan JM, Rauenzahn KA (1987) Frictional dependence of gouge mixtures of quartz and montmorillonite on velocity, composition, and fabric. *Tectonophysics* 144:87–108, doi:10.1016/0040-1951(87)90010-2
- Marone C, Hobbs BE, Ord A (1992) Coulomb constitutive laws for friction: contrasts in frictional behavior for distributed and localized shear. *Pure Appl Geophys* 139:195–214, doi:10.1007/BF00876327
- Matsumura M, Hashimoto Y, Kimura G, Ohmori-Ikehara K, Enjoji M, Ikesawa E (2003) Depth of oceanic crust underplating in subduction zone – inference from fluid inclusion analysis of crack-seal veins. *Geology* 31:1005–1008, doi:10.1130/G19885-1

- Moore JC, Saffer D (2001) Updip limit of the seismogenic zone beneath the accretionary prism of southwest Japan: an effect of diagenetic to low-grade metamorphic processes and increasing effective stress. *Geology* 29:183–186
- Moore GF, Bangs NL, Taira A, Kuramoto S, Pangborn E, Tobin HJ (2007) Three-dimensional splay fault geometry and implications for tsunami generation. *Science* 318(5853):1128–1131, doi:10.1126/science.1147195
- Moore GF, Park J-O, Bangs NL, Gulick SP, Tobin HJ, Nakamura Y, Sato S, Tsuji T, Yoro T, Tanaka H, Uraki S, Kido Y, Sanada Y, Kuramoto S, Taira A (2009) Structural and seismic stratigraphic framework of the NanTroSEIZE stage 1 transect. In: Kinoshita M, Tobin H, Ashi J, Kimura G, Lallemand S, Screation EJ, Curewitz D, Masago H, Moe KT, the Expedition 314/315/316 Scientists, Proc. IODP, 314/315/316. Integrated Ocean Drilling Program Management International, Inc, Washington, DC, doi:10.2204/iodp.proc.314315316.102.2009
- Morgan JK, Ask MVA (2004) Consolidation state and strength of underthrust sediments and evolution of the décollement at the Nankai accretionary margin: results of uniaxial reconsolidation experiments. *J Geophys Res* 109:B03102, doi:10.1029/2002JB002335
- Morgan JK, Karig DE (1995) Décollement processes at the Nankai accretionary margin, southeast Japan: propagation, deformation and dewatering. *J Geophys Res* 100:15221–15231
- Oleskevich DA, Hyndman RD, Wang R (1999) The updip and downdip limits to great subduction earthquakes: thermal and structural models of Cascadia, south Alaska, SW Japan, and Chile. *J Geophys Res* 104:14965–14991
- Park JO, Kodaira S (2012) Seismic reflection and bathymetric evidences for the Nankai earthquake rupture across a stable segment-boundary. *Earth Planets Space* 64:299–303, doi:10.5047/eps.2011.10.006
- Park JO, Tsuru T, Kodaira S, Cummins PR, Kaneda Y (2002) Splay fault branching along the Nankai subduction zone. *Science* 297:1157–1160
- Reid HF (1911) The elastic-rebound theory of earthquakes. *Bulletin of the Department of Geology*, vol 6. University of California Publications, pp 413–444
- Richter D (1989) *Ingenieur- und Hydrogeologie*. Walter de Gruyter, Berlin
- Rietveld HM (1969) A profile refinement method for nuclear and magnetic structures. *J Appl Crystallogr* 2:65–71
- Roller S, Pohl C, Behrmann JH (2003) 17. Data report: triaxial shear strength investigation of sediments and sedimentary rocks from the Japan trench, ODP Leg 186. In: Suyehiro K, Sacks IS, Acton GD, Oda M (eds) *Proceedings of the Ocean Drilling Program, scientific results*, vol 186, College Station
- Saffer DM, Marone C (2003) Comparison of smectite- and illite-rich gouge frictional properties: application to the updip limit of the seismogenic zone along subduction megathrusts. *Earth Planet Sci Lett* 215:219–235, doi:10.1016/S0012-821X(03)00424-2
- Saffer DM, Tobin HJ (2011) Hydrogeology and mechanics of subduction zone forearcs: fluid flow and pore pressure. *Annu Rev Earth Planet Sci* 39:157–186, doi:10.1146/annurev-earth-040610-133408
- Saito S (1992) Stratigraphy of Cenozoic strata in the southern terminus area of Boso Peninsula, central Japan. *Contributions of Institute of Geology and Paleontology, Tohoku University*, vol 93:1–37
- Savage JC, Byerlee JD, Lockner DA (1997) Is internal friction friction? *Geophys Res Lett* 23:1944–8007, doi:10.1029/96GL00241
- Scholz CH (1998) Earthquakes and friction laws. *Nature* 391:37–42
- Schumann K (2014) Strength, textures, microfabrics and acoustic properties of active plate margin sediments on- and offshore SW Japan. Dissertation, Christian-Albrechts-Universität zu Kiel, p 341
- Schumann K, Stipp M, Leiss B, Behrmann JH (2014) Texture development of naturally compacted and experimentally deformed silty clay sediments from the Nankai Trench and Forearc, Japan. *Tectonophysics*, doi:10.1016/j.tecto.2014.08.005
- Skarbak RM, Saffer DM (2009) Pore pressure development beneath the décollement at the Nankai subduction zone: implications for plate boundary fault strength and sediment dewatering. *J Geophys Res* 114:B07401, doi:10.1029/2008JB006205
- Stipp M, Rolfs M, Behrmann JH, Schumann K, Schulte-Kortnack D, Feeser V (2013) Strong sediments at the deformation front, and weak sediments at the rear of the Nankai accretionary prism, revealed by triaxial deformation experiments. *Geochem Geophys Geosyst* 14: doi:10.1002/ggge.20290
- Taira A, Okada H, Whitaker JH, Smith AJ (1982) The Shimanto Belt of Japan: cretaceous-lower Miocene active-margin sedimentation. *Geol Soc Lond, Spec Publ* 10:5–26
- Taira A, Katto J, Tashiro M, Okamura M, Kodama K (1988) The Shimanto Belt in Shikoku, Japan: evolution of Cretaceous to Miocene accretionary prism. *Mod Geol* 12:5–46
- Taira A, Hill I, Firth J, Berner U, Brückmann W, Byrne T, Chabernaud T, Fisher A, Foucher J-P, Gamo T, Gieskes J, Hyndman R, Karig D, Kastner M, Kato Y, Lallemand S, Lu R, Maltman A, Moore G, Moran K, Olafsson G, Owens W, Pickering K, Siena F, Taylor E, Underwood M, Wilkinson C, Yamano M, Zhang J (1992) Sediment deformation and hydrogeology of the Nankai Trough accretionary prism: synthesis of shipboard results of ODP Leg 131. *Earth Planet Sci Lett* 109:431–450
- Tobin HJ, Kinoshita M (2006a) NanTroSEIZE: the IODP Nankai Trough seismogenic zone experiment. *Sci Drill* 2:23–27, doi:10.2204/iodp.sd.2.06.2006
- Tobin HJ, Kinoshita M (2006b) Investigation of seismogenesis at the Nankai Trough, Japan. IODP Scientific Prospectus, NanTroSEIZE stage 1, doi:10.2204/iodp.sp.nantroseite.1.2006
- Toriumi M, Teruya J (1988) Tectono-metamorphism of the Shimanto Belt. *Mod Geol* 12:303–324
- Twiss RJ, Moores EM (1992) *Structural geology*. Freeman, New York
- Underwood MB (2007) Sediment inputs to subduction zones: why lithostratigraphy and clay mineralogy matter. In: Dixon TH, Moore JC (eds) *The seismogenic zone of subduction thrust faults*. Columbia University Press, New York, pp 42–85
- Underwood MB, Laughland MM, Byrne T, Hibbard JP, DiTullio L (1992) Thermal evolution of the Tertiary Shimanto Belt, Muroto Peninsula, Shikoku, Japan. *Island Arc* 1:116–132
- Underwood MB, Hibbard JP, DiTullio L (1993a) Geologic summary and conceptual framework for the study of thermal maturity within the Eocene-Miocene Shimanto Belt, Shikoku, Japan. In: Underwood MB (ed) *Thermal evolution of the tertiary Shimanto Belt, Southwest Japan: an example of ridge-trench interaction*. Geological Society of America, special paper 273
- Underwood MB, Hibbard JP, DiTullio L (1993b) A comparison among organic and inorganic indicators of diagenesis and low-temperature metamorphism, Tertiary Shimanto Belt, Shikoku, Japan. In: Underwood MB (ed) *Thermal evolution of the tertiary Shimanto Belt, Southwest Japan: an example of ridge-trench interaction*. Geological Society of America, special paper 273
- Underwood MB, Byrne T, Hibbard JP, DiTullio L, Laughland MM (1993c) The effect of ridge subduction on thermal structure of accretionary prisms: a tertiary example from the Shimanto Belt of Japan. In: Underwood MB (ed) *Thermal evolution of the tertiary Shimanto Belt, Southwest Japan: an example of ridge-trench interaction*. Geological Society of America, special paper 273
- Von Huene R, Scholl DW (1991) Observations at convergent margins concerning sediment subduction, subduction erosion, and the growth of continental crust. *Reviews of Geophysics* 29:279–316
- Vrolijk P (1990) On the mechanical role of smectite in the subduction zones. *Geology* 18:703–707
- Yamamoto Y (2006) Systematic variation of shear-induced physical properties and fabric in the Miura-Boso accretionary prism: the earliest processes during off-scraping. *Earth Planet Sci Lett* 244:270–284, doi:10.1016/j.epsl.2006.01.049
- Yamamoto Y, Kawakami S (2005) Rapid tectonics of the Late Miocene Boso accretionary prism related to the Izu-Bonin arc collision. *Island Arc* 14:178–198
- Yamamoto Y, Mukoyoshi H, Ogawa Y (2005) Structural characteristics of shallowly buried accretionary prism: rapidly uplifted Neogene accreted sediments on the Miura-Boso Peninsula, central Japan. *Tectonics* 24:17, doi:10.1029/2005TC001823
- Yamamoto Y, Chiyonobu S, Kurihara T, Yamaguchi Y, Hina S, Hamahashi M, Raimbourg H, Augier R, Gadenne L (2012) Unconformity between a Late Miocene–Pliocene accretionary prism (Nishizaki Formation) and Pliocene trench-slope sediments (Kagamigaura Formation), central Japan. *Island Arc* 21:231–234

doi:10.1186/1880-5981-66-129

**Cite this article as:** Schumann *et al.*: Geotechnical behavior of mudstones from the Shimanto and Boso accretionary complexes, and implications for the Nankai accretionary prism. *Earth, Planets and Space* 2014 **66**:129.